COMMUNICATION

# Integrated Molecular, Interfacial, and Device Engineering towards High-Performance Non-Fullerene Based Organic Solar Cells

*Yue Zang, Chang-Zhi Li, Chu-Chen Chueh, Spencer T. Williams, Wei Jiang, Zhao-Hui Wang,* Jun-Sheng Yu,* and Alex K.-Y. Jen**

Organic solar cells (OSCs) composed of non-fullerene acceptors (denoted as non-fullerene OSCs hereafter) have recently attracted significant attention because they offer possibilities to fabricate devices with materials that can be synthesized easily with versatile functional groups to tune their optical and electronic properties.[1–5] By using non-fullerene acceptors in devices, it can also avoid the drawbacks of fullerenes, including the need for tedious purification, limited light absorption, and chemical and electronic diversities.[6–9]

Among the non-fullerene acceptors exploited so far for OSCs, naphthalene- and perylene tetracarboxylic diimide (NDI and PDI)-based derivatives are the most frequently explored ones due to their simplicity in synthesis, easy-to-tune energy levels, and relatively high electron mobilities.[9] For instance, the NDI-bithiophene-based copolymer (PNDI2OD-T2) has been incorporated in bulk-heterojunction (BHJ) devices to exhibit power conversion efficiencies (PCEs) of over 6%.[10] Small PDI molecule-based BHJ devices have also been shown to reach PCEs of ca. 4%.[11–13] These encouraging results have inspired vigorous development of non-fullerene acceptors aiming at improving device performance to be comparable or better than those derived from their fullerene counterparts.[14–21] Although the efficiency of devices based on small-molecule non-fullerene acceptors are currently lower than their polymer counterparts, they hold the advantages of easier accessibility and purification that warrants better reproducibility.

In addition to developing suitable non-fullerene organic semiconductors, the proper selection of matched donor materials is also very critical for making high-PCE solar cells. There are several important parameters that need to be simultaneously considered to achieve high-performance non-fullerene OSCs such as: i) suitable frontier energy levels from both donor and acceptor semiconductors to facilitate effective photocharge generation, ii) complementary absorption spectra between the donor–acceptor pair to achieve optimal light harvesting, and, iii) proper miscibility to form nanoscale phase-separated morphologies with bicontinuous pathways of donor/acceptor domains for efficient charge transport and collection. To date, the most commonly studied donor polymers for non-fullerene OSCs are poly(3-hexylthiophene) (P3HT) and poly({4,8-bis[(2-ethylhexyl)oxy]benzo[1,2-b:4,5-b′]dithiophene-2,6-diyl}{3-fluoro-2-[(2-ethylhexyl)-carbonyl]-thieno[3,4-b]thiophenediyl}) (PTB7) because they fulfill most of the above-mentioned criteria.[22–25]

Recently, pseudo-two-dimensional (2D) conjugated polymers with alkylthienyl side chains such as PBDTTT-C-T have been shown to achieve improved morphology and charge transport in their BHJ blends with $PC_{71}BM$, which resulted in enhanced device performance.[26] When it was blended with a simple bay-linked perylene bisimide (di-PBI), the resulting device also showed a quite respectable PCE of ca. 3.63%.[27] The improved polymer chain packing and charge transport from this type of donor polymer are attractive because most of the non-fullerene acceptors that have been developed so far lack the 3D charge-transporting characteristics of fullerenes. Since the absorption of di-PBI is below 600 nm, it is also possible to further enhance the PCE of non-fullerene OSCs by introducing narrow band-gap donor polymers with complementary absorption and matched energy levels to ensure high current density and open-circuit voltage.

In this study, we combine molecular, interfacial, and device engineering to demonstrate highly efficient non-fullerene OSCs with PCEs of up to ca. 6.0% based on the blends of a bay-linked di-PBI acceptor (A) with a commercially available pseudo-2D donor polymer PBDTT-F-TT (**Figure 1**). PBDTT-F-TT was selected because of its deeper HOMO and red-shifted absorption that form a better match with di-PBI compared to those for PBDTTT-C-T. The inverted device architecture was chosen because the results from optical modeling show it offers better optical field distribution and exciton generation. In addition,

Y. Zang, Dr. C.-Z. Li, Dr. C.-C. Chueh, S. T. Williams, Prof. A. K.-Y. Jen
Department of Materials Science and Engineering
University of Washington
Box 352120, Seattle, Washington 98195, USA
E-mail: ajen@u.washington.edu
Y. Zang, Prof. J.-S. Yu
State Key Laboratory of Electronic Thin Films and Integrated Devices
School of Optoelectronic Information
University of Electronic Science and Technology of China (UESTC)
Chengdu 610054, PR China
E-mail: jsyu@uestc.edu.cn
Dr. W. Jiang, Prof. Z.-H. Wang
State Key Laboratory of Organic Solids
Beijing National Laboratory for Molecular Sciences
Institute of Chemistry
Chinese Academy of Sciences
Beijing 100190, PR China
E-mail: wangzhaohui@iccas.ac.cn

**DOI: 10.1002/adma.201401992**

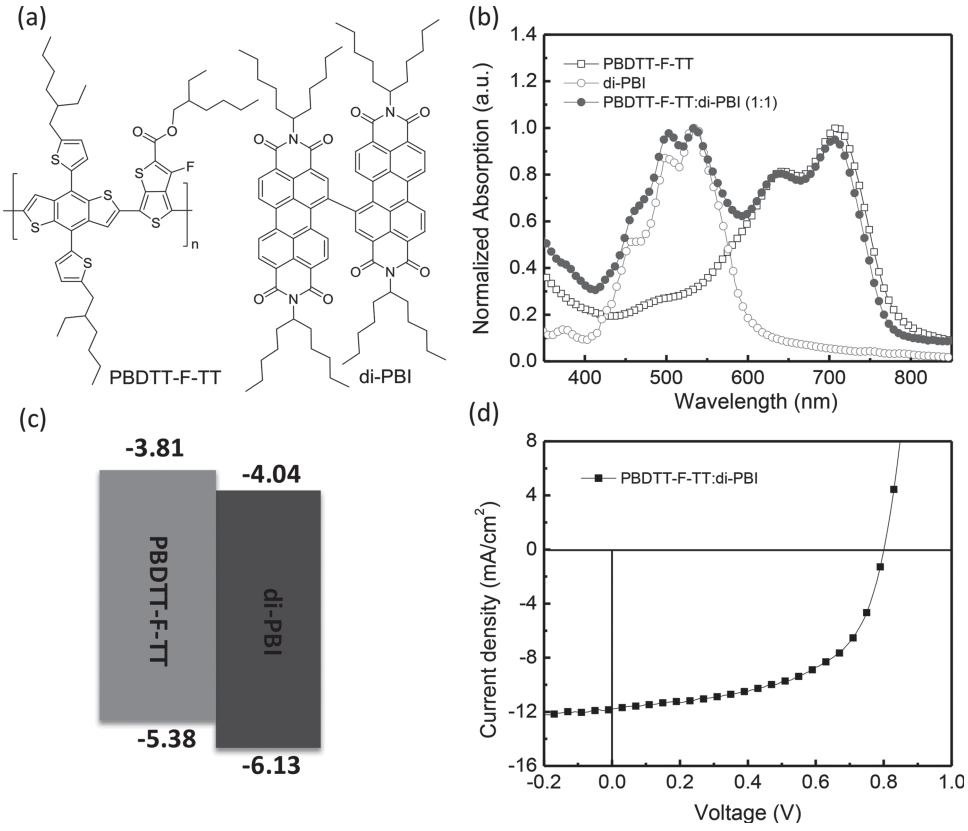


**Figure 1.** a) The chemical structures, b) normalized absorption in solid film state, and, c) energy-level diagram of PBDTT-F-TT and di-PBI; d) *J–V* characteristics of the PBDTT-FTT:di-PBI BHJ-based device with inverted structure of ITO (120 nm)/ZnO (30 nm)/BHJ (105 nm)/$MoO_3$ (8 nm)/Ag (100 nm).

the performance of the device can be significantly improved with a fullerene self-assembled monolayer ($PC_{61}BM$-SAM)-modified zinc oxide (ZnO) interlayer to enhance charge extraction. Finally, non-halogenated solvent was used to demonstrate the feasibility of fabricating large-area devices with high PCE.

The HOMO energy level of PBDTT-F-TT was estimated to be around –5.38 eV by cyclic voltammetry (CV; as shown in Figure 1c), which is lower than that of PBDTTT-C-T. The low-lying HOMO energy level of PBDTT-F-TT should lead to higher $V_{OC}$ for the non-fullerene OSC. The absorption spectra of PBDTT-F-TT and di-PBI are shown in Figure 1b. Di-PBI with an intense absorption band between 400 and 600 nm complements well the absorption of PBDTT-F-TT, which has an intense band between 600–750 nm. The combined absorption between PBDTT-F-TT and di-PBI covers a broad spectrum that will benefit the light harvesting of devices.

To investigate the photovoltaic performance of devices made from di-PBI and PBDTT-F-TT, inverted devices were fabricated with the configuration ITO/ZnO (ca. 30 nm)/PBDTT-F-TT:di-PBI/$MoO_3$ (8 nm)/Ag (100 nm). The solvent additives 1,8-diiodooctane (DIO) and 1-chloronaphthalene (CN) were explored to ensure the BHJ layer has optimal morphology.[28–30] As shown in Figure S1 and Table S1 (see the Supporting Information, SI) for the exemplified PBDTT-F-TT:di-PBI BHJ, the photovoltaic properties can be significantly improved by using binary additives with 1.0% DIO and 2.0% CN in *ortho*-dichorobenzene (*o*-DCB) (v/v). The enhanced short circuit current density ($J_{SC}$) and fill factor (FF) suggest that these additives help optimize BHJ morphology.

The bright-field transmission electron microscopy (TEM) images shown in Figure S2 (see the SI) indicate that the thin film of PBDTT-F-TT:di-PBI processed with binary additives exhibits distinctly enhanced phase separation with well-connected polymer and di-PBI domains. The STEM EDS analysis demonstrates that compositional difference contributes to the contrast we observe (Figure S2c). It indicates that areas of dark contrast in the bright-field images are polymer rich and areas of bright contrast are rich in di-PBI. The significant increase in contrast upon the addition of additives indicates more dramatic phase segregation. This morphology change may facilitate efficient charge dissociation and transport.[22] These optimized conditions are employed for further device studies of the PBDTT-F-TT:di-PBI BHJ.

The current density–voltage (*J–V*) characteristics of the inverted devices under illumination are shown in Figure 1d. $V_{OC}$, $J_{SC}$, FF, and PCE data obtained from the *J–V* curves are summarized in **Table 1**. The PBDTT-F-TT:di-PBI-based BHJ further increases the PCE to (5.28 ± 0.03)% with a $V_{OC}$ of 0.80 ± 0.01 V, a $J_{SC}$ of 11.68 ± 0.17 mA $cm^{-2}$, and a FF of 0.55 ± 0.01. These device performances were significantly improved compared with the previously reported value (3.63%) for PBDTTT-C-T:di-PBI-based devices. The devices with PBDTT-F-TT as donor have a significantly higher $V_{OC}$ (0.80 V) than the devices with PBDTTT-C-T (0.72 V), which is consistent

**Table 1.** Comparison of performance parameters of the conventional and inverted structure devices based on PBDTT-F-TT:di-PBI BHJ.

| Device | $V_{OC}$ [V] | $J_{SC}$ [mA cm$^{-2}$] | FF | PCE [%][a)] | $\sigma_{mean}$[b)] | $R_S$ [Ω cm$^2$] | $R_P$ [kΩ cm$^2$] | $J_S$ [mA cm$^{-2}$] | $n$ |
|---|---|---|---|---|---|---|---|---|---|
| Conventional | 0.76 ± 0.01 | 10.22 ± 0.39 | 0.51 ± 0.01 | 4.21 (4.04) | 2.7% | – | – | – | – |
| Inverted | 0.80 ± 0.01 | 11.68 ± 0.17 | 0.55 ± 0.01 | 5.31 (5.28) | 1.1% | 0.74 | 29.40 | $2.20 \times 10^{-8}$ | 1.66 |
| Inverted (SAM) | 0.80 ± 0 .01 | 11.98 ± 0.34 | 0.59 ± 0.01 | 5.90 (5.73) | 2.1% | 1.69 | 49.88 | $3.44 \times 10^{-9}$ | 1.50 |

[a)]Average PCE in brackets; [b)]Error values represent the standard deviation of the mean of 8 devices.

with its deeper HOMO energy level. The higher $J_{SC}$ and FF may derive from better light harvesting and balanced charge dissociation and transport enabled by the enhanced phase separation.

We found that device configuration (shown in **Figure 2**a) has great influence on the overall performance of the PBDTT-F-TT:di-PBI-based devices. Figure S3a (see the SI) and Table 1 showed that the average PCE of the inverted device ((5.28 ± 0.03)%) is much higher than that of the conventional one ((4.04 ± 0.07)%). All parameters are improved in the inverted configuration, especially the $J_{SC}$ which is evident in the external quantum efficiencies (EQEs) shown in Figure 2b. The EQE curves reveal that the inverted device has superior light conversion in the region between 500 and 800 nm compared to that of the conventional device (Figure 1b). It is worth noting that the peak value of over 50% at around 500 nm is among the highest EQE reported for non-fullerene OSCs. The surface morphology of the PBDTT-F-TT:di-PBI BHJ was examined by atomic force microscopy (AFM; Figure S4). It was found that the optimized morphology on PEDOT:PSS (in the conventional configuration) or ZnO (in the inverted configuration) is very similar and shows comparable root-mean-square (RMS) surface roughness (3.03 and 3.81 nm for PEDOT:PSS/BHJ and ZnO/BHJ, respectively). This result excludes the possible contribution from BHJ morphology on the divergent performance under different device configuration.

The light-harvesting properties of BHJ in different device architectures is another dominant factor that governs the exciton generation of devices. For instance, the light-absorbing intensity of the BHJ films is influenced by the refractive index of the each layer in the device due to the interference effect. To evaluate the optical profiles of different device geometries, optical modeling based on the transfer matrix method (TMM) was used to calculate the interference of reflected and transmitted light at each interface of the device.[31] All the needed optical constants for simulation were measured by spectroscopic ellipsometry and the resultant wavelength-dependent complex index of refraction ($n$ + i$k$) of each material is presented in Figure S5 (see the SI). The simulated fractions of light absorbed by BHJ layers in both conventional and inverted device structures are plotted in Figure 2b. The results show that the inverted device has a more intense absorption fraction than the conventional one due to different sequence and optical properties of each composing interlayer, which is consistent with the enhanced EQE. It demonstrates that better light

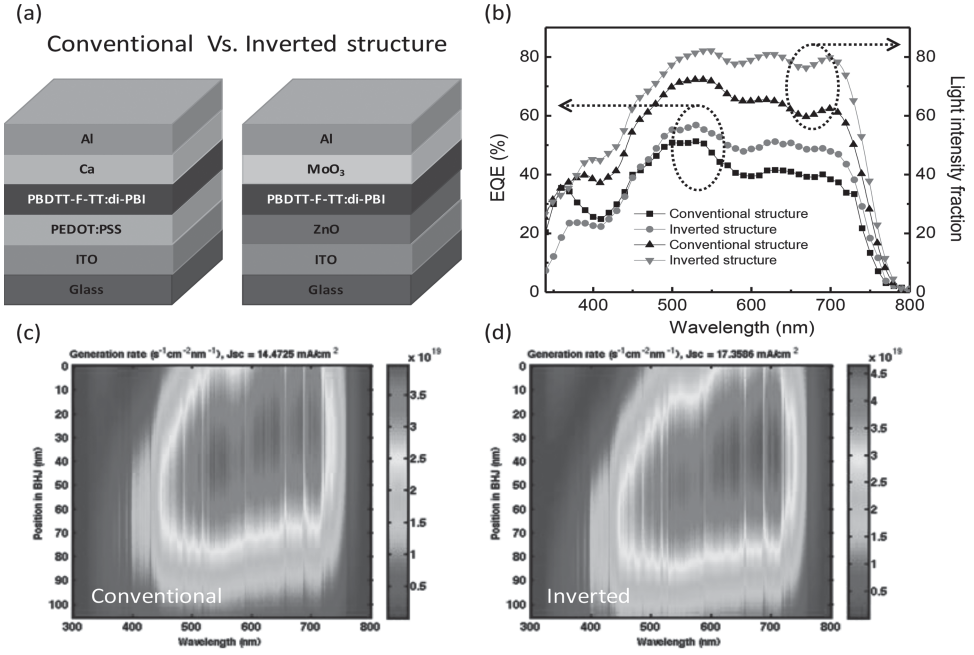


**Figure 2.** a) Schematic illustration of the studied device configurations, b) EQE spectra and calculated fraction of absorbed light intensity, and, c,d) calculated wavelength dependence of exciton generation rate of PBDTT-F-TT:di-PBI BHJ devices in conventional (ITO (120)/PEDOT:PSS (30 nm)/BHJ (105 nm)/Ca (20 nm)/Al (100 nm)) and inverted (ITO (120 nm)/ZnO (30 nm)/BHJ (105 nm)/$MoO_3$ (8 nm)/Ag (100 nm)) structures.

absorption in the inverted device contributes to its superior performance to the conventional one.

In addition to light harvesting, the distribution of photogenerated excitons in different device structures also has great influence on charge transport and collection. The spatial distribution of exciton generation in the photoactive layer is simulated and illustrated in Figures 2c–d, and S3b. Due to the higher fraction of absorbed light, the inverted device shows higher exciton generation than the conventional device. Notably, the generated excitons in the inverted device are broadly distributed with a peak centered at the BHJ layer, while the excitons in the conventional device are more concentrated near the ITO anode with their peak much farther away from the cathode. This suggests that more balanced charge transport can be achieved in the inverted device.

Based on this finding, the carrier mobility of the BHJ layer was measured using the space charge-limited current (SCLC) technique (Figure S6 in the SI). The estimated electron mobility ($\mu_e$) from the *J–V* curve characteristics for the electron-only device is around $3.32 \times 10^{-5}$ cm$^2$ V$^{-1}$ s$^{-1}$, which is 3 orders of magnitude lower than that for hole mobility ($\mu_h$ = $4.36 \times 10^{-2}$ cm$^2$ V$^{-1}$ s$^{-1}$). The shifted exciton generation profile towards the cathode in the inverted devices compensates for the poor electron mobility in the BHJ, which reduces charge recombination. Therefore, it can be concluded from both optical modeling and SCLC results that better optical distribution in the inverted device contributes to the increased $J_{SC}$ and FF compared to the conventional device.

With the abovementioned results in hand, we focus on optimizing the interface of inverted devices to further improve their performance. Previously, we have demonstrated that $C_{60}$-SAM can be used to modify the ZnO electron selective layer to achieve more than 25% improvement of PCE in P3HT:$PC_{61}BM$ BHJ-based inverted device.[32] Such a thin SAM layer not only passivates the charge-trapping hydroxyl groups on ZnO, but also facilitates the charge collection from BHJ to electrode. Based on this, we have modified the ZnO surface with $PC_{61}BM$-SAM to further enhance device efficiency.

The *J–V* characteristics of inverted devices without and with $PC_{61}BM$-SAM under light illumination and in the dark are compared in **Figure 3**a and b. Very encouragingly, the average PCE of the SAM-modified device could be further increased from (5.28 ± 0.03)% to (5.73 ± 0.17)% ($PCE_{max}$ of 5.90%). The enhancement is mainly due to increased FF (from 0.55 to 0.59) and $J_{SC}$ (from 11.68 to 11.93 mA cm$^{-1}$; Figure S7 in the SI). Meanwhile, the standard deviation of the mean ($\sigma_{mean}$) is very small for 8 devices, as shown in Table 1. These results demonstrate the good reproducibility of these non-fullerene based devices. To understand the mechanism for the enhancement by SAM modification, we modeled the dark *J–V* characteristics of the corresponding devices with the Shockley diode equation:

$$J_{Dark} = J_S \left\{ \exp\left[ \frac{V - JR_S A}{nkT/q} \right] - 1 \right\} + \frac{V - JR_S A}{R_P A} \quad (1)$$

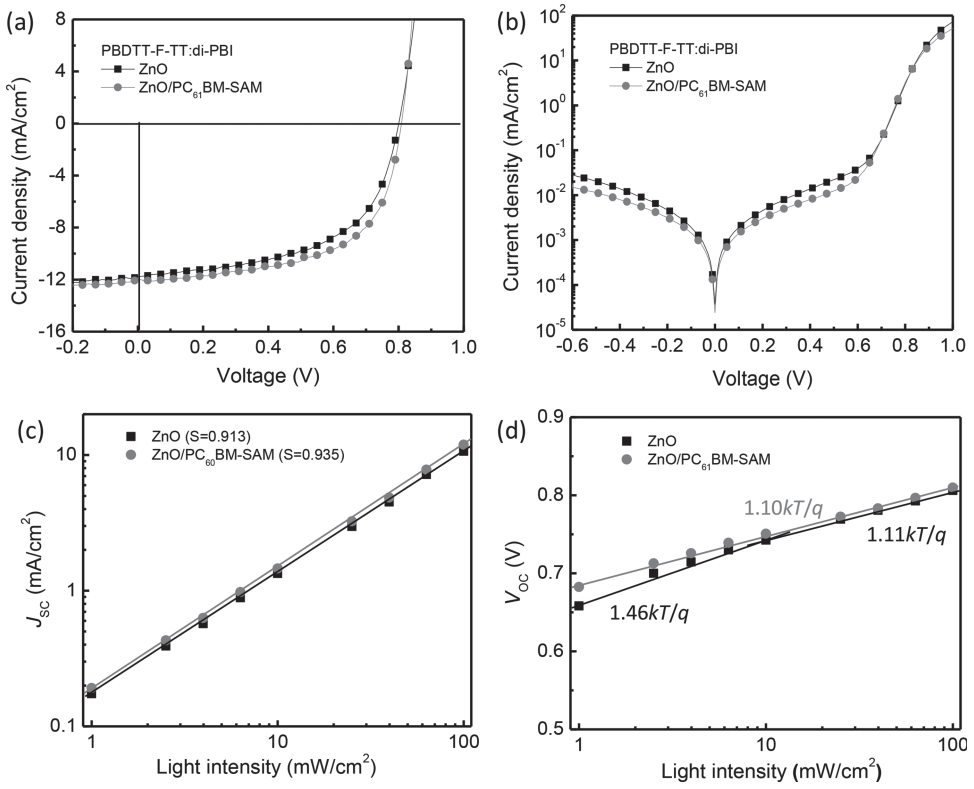


**Figure 3.** *J–V* characteristics: a) under illumination, and, b) in the dark; and, light-intensity dependence of: c) $J_{SC}$, and, d) $V_{OC}$ of PBDTT-F-TT:di-PBI BHJ-based inverted structure devices without and with $PC_{61}BM$-SAM modification: ITO (120 nm)/ZnO (30 nm)/$PC_{61}BM$-SAM (w/o or w)/BHJ (105 nm)/$MoO_3$ (8 nm)/Ag (100 nm).

where $q$ is the electron charge, $k$ is Boltzmann's constant, and $T$ is the temperature. The relevant diode parameters, including series resistance ($R_S$), shunt resistance ($R_P$), reverse saturation current density ($J_S$), and ideal factor ($n$), are summarized in Table 1. Both the increased $R_P$ (from 29.40 to 49.88 kΩ cm$^2$) and decreased $J_S$ (from $2.20\times10^{-8}$ to $3.44\times10^{-9}$ mA cm$^{-2}$) of the devices affirm that the $PC_{61}BM$-SAM effectively enhances electron selectivity and reduces charge recombination losses at the interface between the ZnO and BHJ layers.

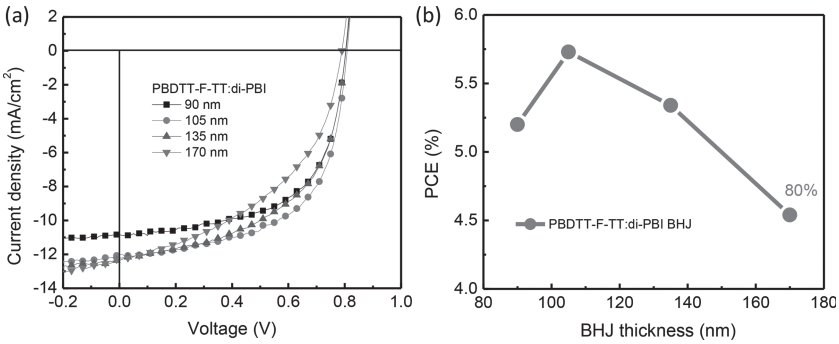


**Figure 4.** a) *J–V* characteristics of PBDTT-F-TT:di-PBI-based inverted structure devices with different active layer thicknesses; and, b) thickness dependence of PCE in PBDTT-F-TT:di-PBI-based non-fullerene OSCs.

It is well known that the dependence of *J–V* characteristics on light intensity ($P_0$) can provide useful information on the recombination loss of devices and this has been widely used to describe the monomolecular and/or bimolecular recombination.[33,34] Monomolecular recombination refers to any first-order process including the geminate recombination of a bound electron–hole pair before dissociation and the Shockley-Read-Hall (SRH) recombination through the shallow traps created by interfacial defects and/or impurities in materials. Bimolecular recombination refers to the recombination of free electrons and holes in the BHJ layer.

Since the generated excitons will be swept out prior to recombination under short-circuit condition, bimolecular recombination can be considered negligible. This will result in a linear dependence of $J_{SC}$ on the light intensity with a slope close to 1. Figure 3c shows the dependence of $J_{SC}$ on light intensity of the studied devices, in which the fitted slope ($S$) by the power law is 0.91 and 0.93 for the devices without and with $PC_{61}BM$-SAM modification, respectively. This result shows the SAM-modified interface not only reduces bimolecular recombination in BHJ, but also mitigates recombination loss at the BHJ/electrode interface.

Figure 3d shows the relationship between $V_{OC}$ and light intensity of the studied devices without and with $PC_{61}BM$-SAM modification. In principle, the slope of $V_{OC}$ versus ln($P_0$) will be equal to $kT/q$ if bimolecular recombination is dominant.[33] In the case of trap-assisted SRH recombination, a stronger dependence of $V_{OC}$ on the light intensity will show a slope of $2kT/q$. Notably, the device without SAM modification possesses a strong $V_{OC}$ dependence on light intensity with a slope of 1.46 $kT/q$ at low light intensities while the device with SAM modification shows a unique slope of 1.10 $kT/q$ throughout the entire range of light intensity. This result indicates that traps from the ZnO surface contribute to monomolecular SRH recombination at low light intensities (1 to 10 mW cm$^{-2}$) while the SAM-modified ZnO does not encounter such losses. All these results affirm that the insertion of a $PC_{61}BM$-SAM layer between ZnO and the organic BHJ layer effectively passivates the inorganic surface trap states to suppress interfacial trap-assisted recombination, leading to an improved shunt resistance as well as device performance.

From a practical application point of view, the ability to form a thicker BHJ layer in OPV processing is very critical not only for light harvesting but also for fabricating large-area device with smooth and pin-hole-free organic films. To address this issue, we studied the effect of non-fullerene BHJ thickness on device performance. The performance of inverted devices with varied BHJ thickness is shown in **Figures 4** and S8 (see the SI), and the related parameters are summarized in Table S2.

As shown, the optimized efficiency ((5.73 ± 0.17)%) of PBDTT-F-TT:di-PBI BHJ could be achieved with a BHJ thickness of ca. 105 nm. The $J_{SC}$ of the device rose as the thickness of BHJ increases from 105 to 170 nm. However, the overall PCE decreased due to reduced FF, probably due to poor electron mobility of the BHJ. However, the PBDTT-F-TT:di-PBI device maintained ca. 80% of its PCE value as the BHJ thickness increased from 105 to 170 nm, which suggests that the 2D PBDTT-F-TT can sustain a thicker BHJ layer for efficient charge transport and collection. Finally, an average PCE of (4.47 ± 0.07)% can be achieved in devices with a 170 nm thick BHJ layer, which is among the best results reported for non-fullerene OSCs.

Another challenge for applying OSC inks in roll-to-roll printing is the usage of halogenated aromatic solvents (e.g., chlorobenzene (CB) or *o*-dichlorobenzene (*o*-DCB)), which are harmful and not environmentally friendly.[35,36] To alleviate this problem, we employed non-halogenated solvents such as toluene or xylene to fabricate non-fullerene OSC devices. The processing of polymer/fullerene based devices has been significantly hindered by the poor solubility of fullerenes in non-halogenated solvents, which tends to lower device efficiency due to severe phase separation within the BHJ films.

Due to the better solubility and processability of non-fullerene OSCs in non-halogenated solvents, device processing is facilitated. As shown in Figure S9 and summarized in Table S3 (see the SI), the performance of PBDTT-F-TT:di-PBI BHJ-based devices processed from *o*-xylene showed a quite high PCE of ca. 5.20%, which is comparable to that obtained using *o*-DCB. More importantly, the additive seems to have marginal effect on devices processed from non-halogenated solvents, which further testifies to the advantage of using non-fullerene acceptors for large-scale manufacturing.

In summary, we have demonstrated a high-performance non-fullerene solar cell (with PCE as high as ca. 6%) by using a pseudo-2D conjugated polymer donor and a di-PBI acceptor. In addition to molecular engineering the donor/acceptor pair to obtain complementary absorption and matched frontier energy levels in BHJ, comprehensive device and interface

engineering have resulted in higher device efficiency by using an inverted device configuration with a SAM-modified ZnO interface. Optical modeling using transfer matrix formalism reveals that the better optical field distribution and exciton generation achieved in inverted device plays an important role in enhancing device performance. Moreover, the SAM modification on ZnO was found to prevent trap-assisted recombination at the interface to further enhance device performance. High PCEs were also demonstrated for devices with a thicker BHJ layer (170 nm) and devices fabricated with non-halogenated solvents. These parameters are very important for large-area device fabrication. These combined molecular, interfacial, and device engineering of non-fullerene solar cells provide valuable insights on designing novel materials and devices for efficient organic electronics.

## Experimental Section

*Device Fabrication*: OSCs were fabricated using ITO-coated glass substrates (15 Ω $sq^{-1}$), which were cleaned with detergent, de-ionized water, acetone, and isopropyl alcohol in successive 10 min sonication steps applying a final 20 s oxygen plasma treatment to eliminate any remaining organic component. In the conventional structure devices, a thin layer (ca. 30 nm) of PEDOT:PSS (Baytron P VP Al 4083, filtered at 0.45 μm) was first spin-coated on the pre-cleaned ITO-coated glass substrates at 5000 rpm and baked at 140 °C for 10 min under ambient conditions. The substrates were then transferred into a nitrogen-filled glovebox. Subsequently, the PBDTT-F-TT:di-PBI active layer was spin-coated on the PEDOT:PSS layer from a homogeneous solution. The solution was prepared by dissolving the PBDTT-F-TT and di-PBI with a weight ratio of 1:1 in *o*-DCB overnight and filtering through a PTFE (polytetrafluoroethylene) filter (0.2 μm). Binary solvent additives, 1,8-diiodooctane and 1-chloronaphthalene (DIO and CN), were used to improve the BHJ morphology. At the final stage, the substrates were pumped down in high vacuum ($<2 \times 10^{-6}$ Torr), and calcium (20 nm) topped with aluminium (100 nm) was thermally evaporated onto the active layer. For inverted device fabrication, a thin layer of sol–gel ZnO (ca. 30 nm) was spin-coated onto pre-cleaned ITO-coated glass substrates at 4000 rpm and then annealed at 200 °C for 1 h in air. The ZnO precursor solution was prepared by dissolving zinc acetate dehydrate $C_4H_6O_4Zn{\cdot}2(H_2O)$ (99.5%, Merck 1 g) and monoethanolamine ($HOCH_2CH_2NH_2$, 98% Acros, 0.28 g) in 2-methoxyethanol ($CH_3OCH_2CH_2OH$, Aldrich, 98%, 10 mL) under stirring for 8 h for hydrolysis reaction and aging. $PC_{61}BM$-SAM was deposited on the ZnO surface using a two-step spinning process.[28] The same process used for active layer in the conventional structure devices was also used for the inverted devices. For halogen-free devices, *o*-xylene, and 1-methylnaphthalene (Me-naph) were used as solvent and additive to prepare the active layer. After that, an 8 nm thick $MoO_3$ film and 100 nm Ag were deposited to complete the inverted device structure. Shadow masks were used to define the OSC active area ($3.14 \times 10^{-2}$ $cm^2$) of the devices.

*Device Characterization*: The current density–voltage (*J*–*V*) characteristics of unencapsulated photovoltaic devices were measured under $N_2$ using a Keithley 2400 source meter. A 300 W xenon arc solar simulator (Oriel) with an AM 1.5 global filter operated at 100 mW $cm^{-2}$ was used to simulate the AM 1.5G solar irradiation. The illumination intensity was corrected by using a silicon photodiode with a protective KG5 filter calibrated by the National Renewable Energy Laboratory (NREL). The EQE system uses a lock-in amplifier (Stanford Research Systems SR830) to record the short-circuit current under chopped monochromatic light.

*SCLC Mobility Measurements*: Space charge-limited currents were tested in electron-only devices with a configuration of glass/Al/PBDTT-F-TT:di-PBI/Ca/Al and hole-only devices with a configuration of ITO/PEDOT:PSS/PBDTT-F-TT:di-PBI/$MoO_3$/Ag. The devices were prepared following the same procedure described in the experimental section for photovoltaic devices, except for the metal electrode. The mobilities were determined by fitting the dark current to the model of a single carrier SCLC current with field dependent mobility, which is described as

$$J = \frac{9\varepsilon_r\varepsilon_0\mu_0 V^2}{8L^2}\exp\left(\beta\frac{V}{L}\right) \quad (2)$$

Where *J* is the current, $\mu_0$ is the zero-field mobility, $\varepsilon_0$ is the permittivity of free space, $\varepsilon_r$ is the relative permittivity of the material, *V* is the effective voltage, and *L* is the thickness of the active layer.

*TEM Characterization*: BHJs for TEM analysis were prepared via the same method discussed above for the conventional architecture excluding the deposition of the electrode. These uncompleted devices were carefully immersed into water to dissolve the PEDOT:PSS layer, leaving the bare BHJ floating on the water surface. This film was then mounted on a copper TEM grid without a carbon support film. Bright-field images were acquired with a Tecnai G2 F20 TEM at 120 kV with the use of an objective aperture and a CCD camera detector. STEM EDS measurements were conducted with a HAADF detector at 120 kV.

## Supporting Information

Supporting Information is available from the Wiley Online Library or from the author.

## Acknowledgements

The authors thank the support from the Air Force Office of Scientific Research (No. FA9550-09-1-0426), the Asian Office of Aerospace R&D (No. FA2386-11-1-4072), and the Office of Naval Research (No. N00014-11-1-0300). A.K.-Y.J. thanks the Boeing Foundation for support. Y.Z. thanks the State-Sponsored Scholarship for Graduate Students from China Scholarship Council and Fundamental Research Funds for the Central Universities (No. ZYGX2012YB025). C.-C.C. is grateful for financial support from National Taiwan University (101R4000). S.T.W. is grateful for support from the NSF GRFP (No. 1256082). Z.W. thanks the National Natural Science Foundation of China (21225209) and NSTF-DFG Joint Project TRR61.

Received: May 3, 2014
Revised: May 22, 2014
Published online: June 18, 2014

[1] X. He, F. Gao, G. Tu, D. Hasko, S. Huttner, U. Steiner, N. C. Greenham, R. H. Friend, W. T. Huck, *Nano Lett.* **2010**, *10*, 1302.
[2] J. R. Moore, S. Albert-Seifried, A. Rao, S. Massip, B. Watts, D. J. Morgan, R. H. Friend, C. R. McNeill, H. Sirringhaus, *Adv. Energy Mater.* **2011**, *1*, 230.
[3] Y. Zhou, T. Kurosawa, W. Ma, Y. Guo, L. Fang, K. Vandewal, Y. Diao, C. Wang, Q. Yan, J. Reinspach, J. Mei, A. L. Appleton, G. I. Koleilat, Y. Gao, S. C. B. Mannsfeld, A. Salleo, H. Ade, D. Zhao, Z. Bao, *Adv. Mater.* **2014**, DOI:10.1002/adma.201306242.
[4] Z. H. Lu, B. Jiang, X. Zhang, A. Tang, L. L. Chen, C. L. Zhan, J. N. Yao, *Chem. Mater.* **2014**, DOI: 10.1021/cm5006339.
[5] A. Eftaiha, J.-P. Sun, L. G. Hill, G. C. Welch, *J. Mater. Chem. A* **2014**, *2*, 1201.
[6] C.-Z. Li, H.-L. Yip, A. K.-Y. Jen, *J. Mater. Chem.* **2012**, *22*, 4161.
[7] M. C. Scharber, D. Mühlbacher, M. Koppe, P. Denk, C. Waldauf, A. J. Heeger, C. J. Brabec, *Adv. Mater.* **2006**, *18*, 789.

[8] E. Bundgaard, F. C. Krebs, *Sol. Energy Mater. Sol. Cells* **2007**, *91*, 954.
[9] J. D. Servaites, B. M. Savoie, J. B. Brink, T. J. Marks, M. A. Ratner, *Energy Environ. Sci.* **2012**, *5*, 8343.
[10] A. Facchetti, *Mater. Today* **2013**, *16*, 123.
[11] X. Zhang, Z. H. Lu, L. Ye, C. L. Zhan, J. H. Hou, S. Q. Zhang, B. Jiang, Y. Zhao, J. H. Huang, S. L. Zhang, Y. Liu, Q. Shi, Y. Q. Liu, J. N. Yao, *Adv. Mater.* **2013**, *25*, 5791.
[12] R. Shivanna, S. Shoaee, S. Dimitrov, S. K. Kandappa, S. Rajaram, J. R. Durrant, K. S. Narayan, *Energy Environ. Sci.* **2014**, *7*, 435.
[13] Y. Lin, Y. Wang, J. Wang, J. Hou, Y. Li, D. Zhu, X. Zhan, *Adv. Mater.* **2014**, DOI: 10.1002/adma.201400525.
[14] E. Zhou, J. Cong, K. Hashimoto, K. Tajima, *Adv. Mater.* **2013**, *48*, 6991.
[15] M. Schubert, D. Dolfen, J. Frisch, S. Roland, R. Steyrleuthner, B. Stiller, Z. Chen, U. Scherf, N. Koch, A. Facchetti, D. Neher, *Adv. Energy Mater.* **2012**, *2*, 369.
[16] Y. Zhou, L. Ding, K. Shi, Y.-Z. Dai, N. Ai, J. Wang, J. Pei, *Adv. Mater.* **2012**, *24*, 957.
[17] T. Earmme, Y.-J. Hwang, N. M. Murari, S. Subramaniyan, S. A. Jenekhe, *J. Am. Chem. Soc.* **2013**, *135*, 14960.
[18] P. Cheng, L. Ye, X. Zhao, J. Hou, Y. Li, X. Zhan, *Energy Environ. Sci.* **2014**.*7* 1351
[19] P. E. Schwenn, K. Gui, A. M. Nardes, K. B. Krueger, K. H. Lee, K. Mutkins, H. Rubinstein-Dunlop, P. E. Shaw, N. Kopidakis, P. L. Burn, P. Meredith, *Adv. Energy Mater.* **2011**, *1*, 73.
[20] Y. Zhou, Y.-Z. Dai, Y.-Q. Zheng, X.-Y. Wang, J.-Y. Wang, J. Pei, *Chem. Commun.* **2013**, *49*, 5802.
[21] A. M. Poe, A. M. D. Pelle, A. V. Subrahmanyam, W. White, G. Wantz, S. Thayumanavan, *Chem. Commun.* **2014**, *50*, 2913.
[22] B. C. Thompson, J. M. Fréchet, *Angew. Chem. Int. Ed.* **2008**, *47*, 58.
[23] M. T. Dang, L. Hirsch, G. Wantz, *Adv. Mater.* **2011**, *23*, 3597.
[24] Y. Liang, Z. Xu, J. Xia, S. T. Tsai, Y. Wu, G. Li, C. Ray, L. Yu, *Adv. Mater.* **2010**, *22*, E135.
[25] N. J. Zhou, H. Lin, S. J. Lou, X. G. Yu, P. J. Guo, E. F. Manley, S. Loser, P. Hartnett, H. Huang, M. R. Wasielewski, L. X. Chen, R. P. H. Chang, A. Facchetti, T. J. Marks, *Adv. Energy Mater.* **2014**, *4*, 1300785.
[26] L. J. Hou, S. Q. Zhang, X. Guo, F. Xu, Y. F. Li, J. H. Hou, *Angew. Chem. Int. Ed.* **2011**, *50*, 9697.
[27] W. Jiang, L. Ye, X. G. Li, C. Y. Xiao, F. Tan, W. C. Zhao, J. H. Hou, Z. H. Wang, *Chem. Commum.* **2014**, *50*, 1024.
[28] J. K. Lee, W. L. Ma, C. J. Brabec, J. Yuen, J. S. Moon, J. Y. Kim, K. Lee, G. C. Bazan, A. J. Heeger, *J. Am. Chem. Soc.* **2008**, *130*, 3619.
[29] X. Guo, C. H. Cui, M. J. Zhang, L. J. Huo, Y. Huang, J. H. Hou, Y. F. Li, *Energy Environ. Sci.* **2012**, *5*, 7943.
[30] C. V. Hoven, X.-D. Dang, R. C. Coffin, J. Peet, T.-Q. Nguyen, G. C. Bazan, *Adv. Energy Mater.* **2010**, *22*, E63.
[31] J.-F. Sallinas, H.-L. Yip, C.-C. Chueh, C.-Z. Li, J.-L. Maldonado, A. K.-Y. Jen, *Adv. Mater.* **2012**, *24*, 6362.
[32] S. K. Hau, H.-L. Yip, H. Ma, A. K.-Y. Jen, *Appl. Phys. Lett.* **2008**, *93*, 233304.
[33] S. R. Cowan, A. Roy, A. J. Heeger, *Phys. Rev. B* **2010**, *82*, 245207.
[34] L. J. A. Koster, M. Kemerink, M. M. Wienk, K. Maturová, R. A. J. Janssen, *Adv. Mater.* **2011**, *23*, 1670.
[35] K.-S. Chen, H.-L. Yip, C. W. Schlenker, D. S. Ginger, A. K.-Y. Jen, *Org. Electron.* **2012**, *13*, 2870.
[36] C.-C. Chueh, K. Yao, H.-L. Yip, C.-Y. Chang, Y.-X. Xu, K.-S. Chen, C.-Z. Li, P. Liu, F. Huang, Y. W. Chen, W.-C. Chen, A. K.-Y. Jen, *Energy Environ. Sci.* **2013**, *6*, 3241.